molecules

MDPI

Article

Chiral Jahn–Teller Distortion in Quasi-Planar Boron Clusters

Dongbo Zhao [1,*], Yilin Zhao [2], Tianlv Xu [3], Xin He [4], Shankai Hu [1], Paul W. Ayers [2,*] and Shubin Liu [5,6,*]

1 Institute of Biomedical Research, Yunnan University, Kunming 650500, China
2 Department of Chemistry and Chemical Biology, McMaster University, Hamilton, ON L8S 4M1, Canada
3 College of Chemistry and Chemical Engineering, Hunan Normal University, Changsha 410081, China
4 Qingdao Institute for Theoretical and Computational Sciences, Shandong University, Qingdao 266237, China
5 Research Computing Center, University of North Carolina, Chapel Hill, NC 27599-3420, USA
6 Department of Chemistry, University of North Carolina, Chapel Hill, NC 27599-3290, USA
* Correspondence: dongbo@ynu.edu.cn (D.Z.); ayers@mcmaster.ca (P.W.A.); shubin@email.unc.edu (S.L.)

Abstract: In this work, we have observed that some chiral boron clusters (B_{16}^-, B_{20}^-, B_{24}^-, and B_{28}^-) can simultaneously have helical molecular orbitals and helical spin densities; these seem to be the first compounds discovered to have this intriguing property. We show that chiral Jahn–Teller distortion of quasi-planar boron clusters drives the formation of the helical molecular spin densities in these clusters and show that elongation/enhancement in helical molecular orbitals can be achieved by simply adding more building blocks via a linker. Aromaticity of these boron clusters is discussed. Chiral boron clusters may find potential applications in spintronics, such as molecular magnets.

Keywords: Jahn–Teller effect; helical spin density; helical molecular orbital; boron clusters

1. Introduction

While they are not experimental observables, molecular orbitals are a conceptually useful and elegant tool for elucidating molecular properties [1]. They have long been a significant tool in the arsenal of chemists [2–6], tracing back to the early work of Hückel, Mulliken, and others. One prominent example is the principle of conservation of orbital symmetry [7–9], which subsumes the Woodward–Hoffmann rules. Helical frontier molecular orbitals, first introduced by Hendon et al. [10] in 2013, have seeded a surge of interest. Helical frontier molecular orbitals appear in disubstituted allenes and even-*n* cumulenes. Later, many more types of molecules possessing this interesting property were reported [11–30], and it was discovered that molecules with helical orbitals have interesting physicochemical properties. For example, oligoyne-bridged bifluorenes can induce spin–orbit coupling [30].

Boron forms clusters with unique bonding, aromaticity, and reactivity properties [31–33]. Very recently [34], for the first time, we observed helical spin densities of anionic boron clusters. In this work, we report that B_{16}^- [35], B_{20}^- [36], B_{24}^- [37], and B_{28}^- [38] (see Scheme 1) not only have helical molecular orbitals, but also helical spin densities. This is interesting because, unlike molecular orbitals, spin densities are experimental observables, and this allows the edifice of (spin)-resolved (conceptual) density-functional theory [39–50] to be directly applied to these compounds.

To pin down the origin of spin-density helicity, we forced the quasi-planar boron atoms to be exactly in a plane (where we simply set a column of Cartesian coordinates to zero): helical spin densities are no longer observed. Thus, it is chiral Jahn–Teller distortion that governs the formation of helical spin densities. This seems to be the first observation of this intriguing phenomenon in inorganic boron clusters. We also show that the elongation or enlargement of helical molecular orbitals can be achieved by simply adding more structural motifs via a linker. Moreover, we have exhibited that helical-shape molecules have a large propensity to assume helical molecular orbitals as shown in inorganic species P_9^+ [51], $Be_6B_{11}^-$ [52], and As_{11}^{3-} [53] (vide infra).

check for updates

Citation: Zhao, D.; Zhao, Y.; Xu, T.; He, X.; Hu, S.; Ayers, P.W.; Liu, S. Chiral Jahn–Teller Distortion in Quasi-Planar Boron Clusters. *Molecules* **2024**, *29*, 1624. https://doi.org/10.3390/molecules29071624

Academic Editor: Claudio Fontanesi

Received: 9 February 2024
Revised: 3 April 2024
Accepted: 3 April 2024
Published: 4 April 2024

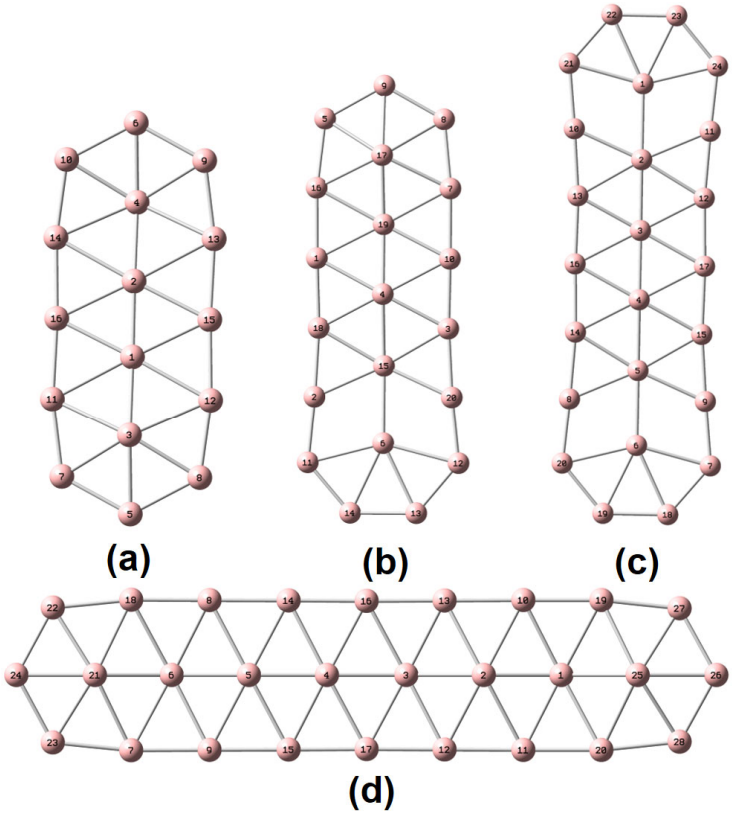

Scheme 1. Molecular representation of (**a**) B_{16}^{-}, (**b**) B_{20}^{-} (**c**) B_{24}^{-} and (**d**) B_{28}^{-} and the corresponding atomic numberings.

2. Results

To characterize the planarity of anionic boron clusters (in both the ground and excited state), we used a few parameters [54], including the molecular planarity parameter (MPP), span of deviation from the plane (SDP), and maximum positive/negative deviation (MPD/MND) to the fitted plane, as listed in Table 1. The definitions of MPP, SDP, MPD, and MND are given in Section 4. The fitted parameters of a plane are listed in Table S1. Of note, in this work, the planarity of a molecule is a geometric concept. Exact planarity means that all the atoms lie in a plane, simply like a benzene molecule. Quasi-planarity indicates that one or more than one atom lie slightly above/below a plane. One can easily discover that all the systems studied in this work are quasi-planar. Based upon the optimized structures in the ground state, we have observed helical spin densities as exhibited in Figure 1. No similar results are discerned for the excited-state structures (see Figure S1).

Table 1. Molecular planarity parameter (MPP), span of deviation from the plane (SDP), maximum positive/negative deviation (MPD/MND) to the fitted plane [a].

Species	MPP	SDP	MPD	MND
$^{2}B_{16}^{-}$	0.090	0.442	0.221	−0.221
$^{4}B_{16}^{-}$	0.017	0.091	0.047	−0.044
$^{2}B_{20}^{-}$	0.081	0.382	0.263	−0.119
$^{4}B_{20}^{-}$	0.083	0.322	0.179	−0.143
$^{2}B_{24}^{-}$	0.021	0.074	0.037	−0.037
$^{4}B_{24}^{-}$	0.039	0.196	0.098	−0.098
$^{2}B_{28}^{-}$	0.092	0.440	0.302	−0.138
$^{4}B_{28}^{-}$	0.103	0.404	0.212	−0.192

[a] Units are in Å.

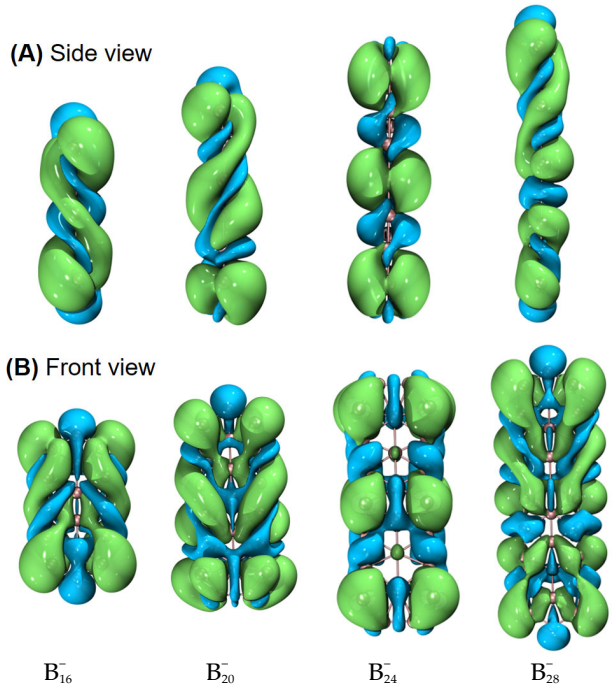

Figure 1. Helical spin densities of quasi-planar boron clusters B_{16}^-, B_{20}^-, B_{24}^-, and B_{28}^- obtained at the PBE0/6-311+G(d) level from both (**A**) side and (**B**) front views. The isovalue was set to be 0.0004 a.u. Molecular renderings were achieved via the VMD 1.9.4 [55] software.

To elucidate the origin of helical spin densities, we force the ground-state quasi-planar boron structures to be exactly planar followed by single-point calculations at the PBE0/6-311+G(d) [56,57] level. The spin densities' helicity then vanishes (see Figure S2). Accordingly, a chiral Jahn–Teller distortion plays a key role where the right- and left-handed deformations are (quasi)equal in energy, and the planar structure deforms slightly to break symmetry, thus lowering in energy. More intriguingly, these chiral structures [in terms of vibrational circular dichroism (VCD) spectra; see Figure 2 for details] can also have helical frontier molecular orbitals as shown in Figure 3. Of note, excited-state VCD spectra are also observed as shown in Figure S3. In the ground state, B_{16}^-, B_{20}^- and B_{28}^- (but not B_{24}^-) have helical β–LUMOs (with lower orbital energies than their α counterparts) and B_{16}^- and B_{20}^- also have helical β–HOMOs in Figure 3; in the excited state, only B_{20}^- and B_{28}^- have helical β–HOMOs. Then, how to understand such a phenomenon?

Our results seem to be specific to π-electron deficient (Be, B) and abundant (P, As) structures, where buckling evidently occurs to accommodate a slight contamination with chirality-supporting sp^3 hybridization. Presumably the difference in these different clusters comes from a delicate balance between a preference for Hückel-esque orbitals and chiral orbitals, which in turn probably reflects electron correlation. We note that the boron cluster with achiral HOMO and LUMO (B_{28}^-) is the least strongly correlated, suggesting that near-degeneracy of the valence orbitals is important for induced chirality. More specifically, the chirality seems to be induced by the type of strong electron correlation that can be modelled with spin-symmetry breaking, which is reflected in the fact that the α and β HOMO and HOMO-1 energies differ quite significantly in B_{16}^- and B_{20}^-, but much less in B_{24}^-. In addition, B_{24}^- has a remarkably large gap between the low-energy β-LUMO and the higher-energy α-LUMO, which perhaps explains its exceptional behavior in Figure 3A.

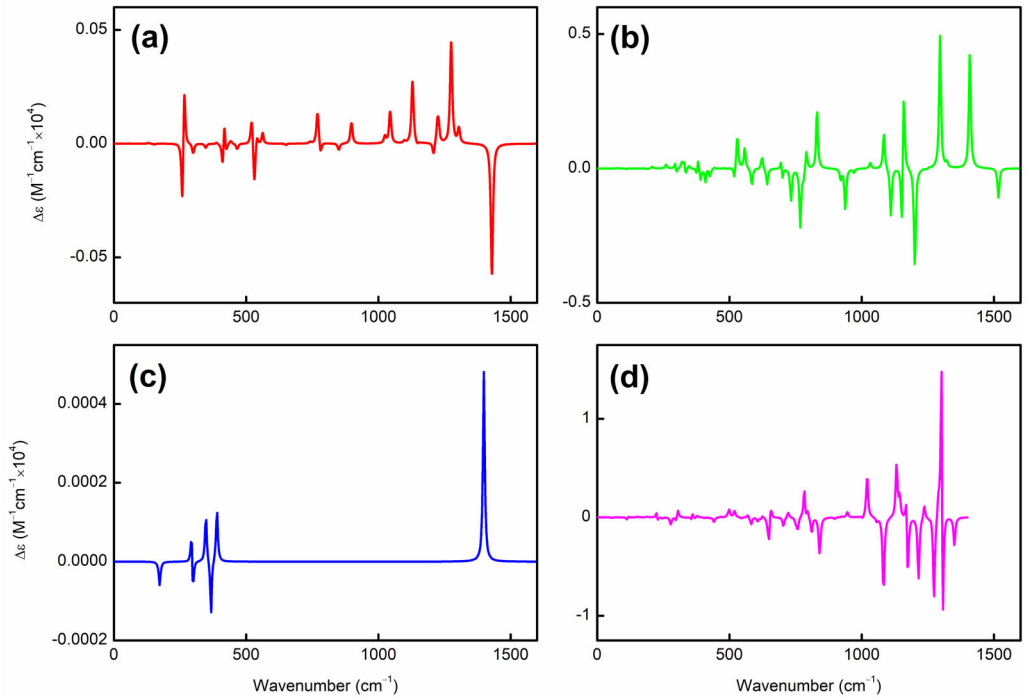

Figure 2. VCD spectra of (**a**) $\mathbf{B_{16}^-}$, (**b**) $\mathbf{B_{20}^-}$, (**c**) $\mathbf{B_{24}^-}$, and (**d**) $\mathbf{B_{28}^-}$ obtained at the PBE0/6-311+G(d) level. The x/y-axis spans from (**a**) to (**d**).

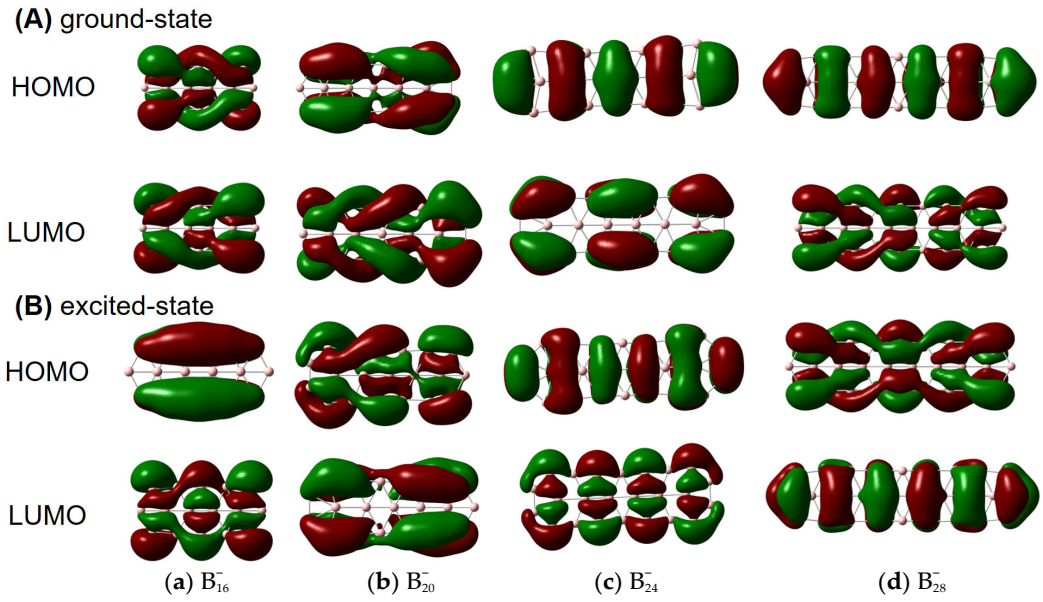

Figure 3. β–HOMOs and β–LUMOs of (**A**) ground- and (**B**) excited-state $\mathbf{B_{16}^-}$, $\mathbf{B_{20}^-}$, $\mathbf{B_{24}^-}$, and $\mathbf{B_{28}^-}$ obtained at the PBE0/6-311+G(d) level from both side and front views. The isovalue was set to be 0.02 a.u. Molecular renderings were achieved via the GaussView 6.0 [58] software.

Figure 4 shows the GIMIC (gauge-including magnetically induced current) [59,60] distributions of both ground- and excited-state B_{16}^-, B_{20}^-, B_{24}^- and B_{28}^-. For $^2B_{16}^-$ and $^4B_{16}^-$, the induced electric currents are running counter-clockwise, which is indicative of aromaticity, as evidenced by the negative NICS (nucleus-independent chemical shift) [61] values as shown in Table 2. Similar results are observed for B_{24}^- and B_{28}^-. However, this is not the case for B_{20}^-. The overall effect indicates that B_{20}^- is antiaromatic while the Z-component of the induced electric current also runs in a counter-clockwise manner as showcased by the $NICS_{ZZ}$ values in Table 2. Yet, the dominant contributions of the induced electric current

lie in the *x*–*y*-plane, which is the source of antiaromaticity. To go a step further, Figure 5 showcases the 3D isotropic shielding surface (ICSS) [62] calculations for both ground- and excited-state boron clusters and it is clearly revealed that there exists a strongly shielded chemical environment along the direction perpendicular to the quasi-planar boron clusters.

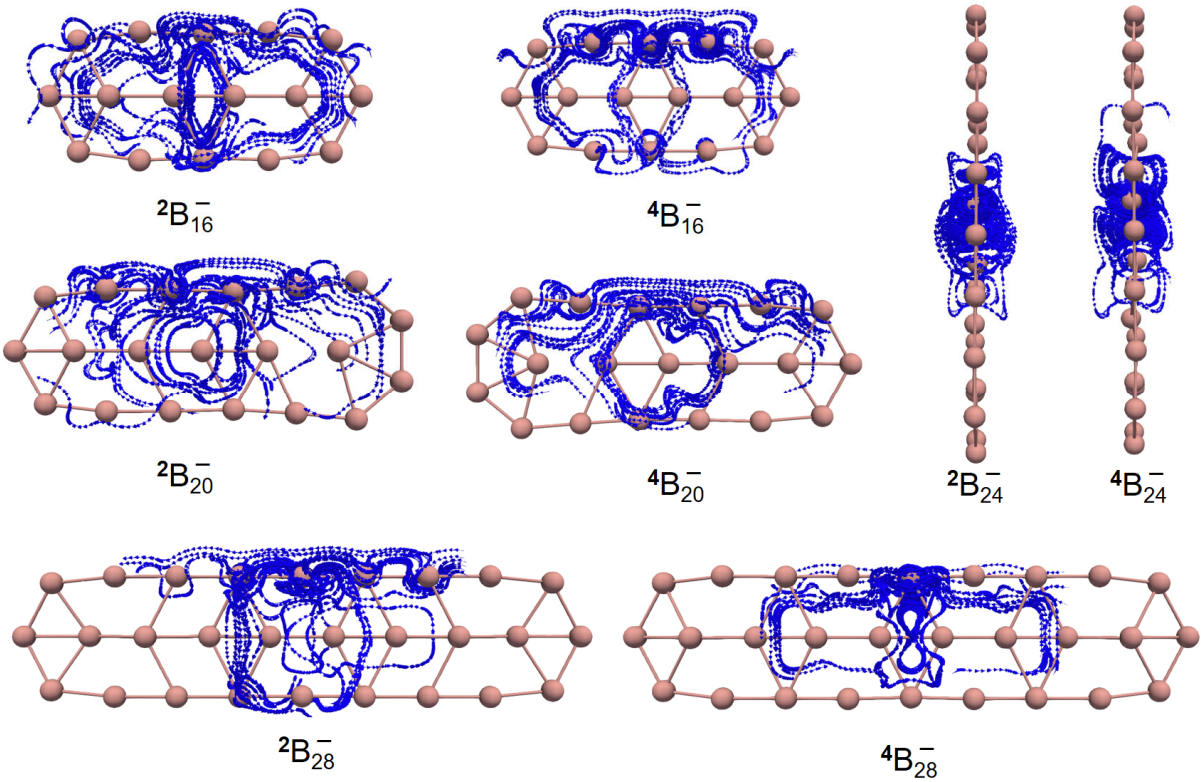

Figure 4. The GIMIC diagrams of both the ground and excited state of B_{16}^-, B_{20}^-, B_{24}^-, and B_{28}^-. Molecular renderings were achieved via the ParaView [63] software (v. 4).

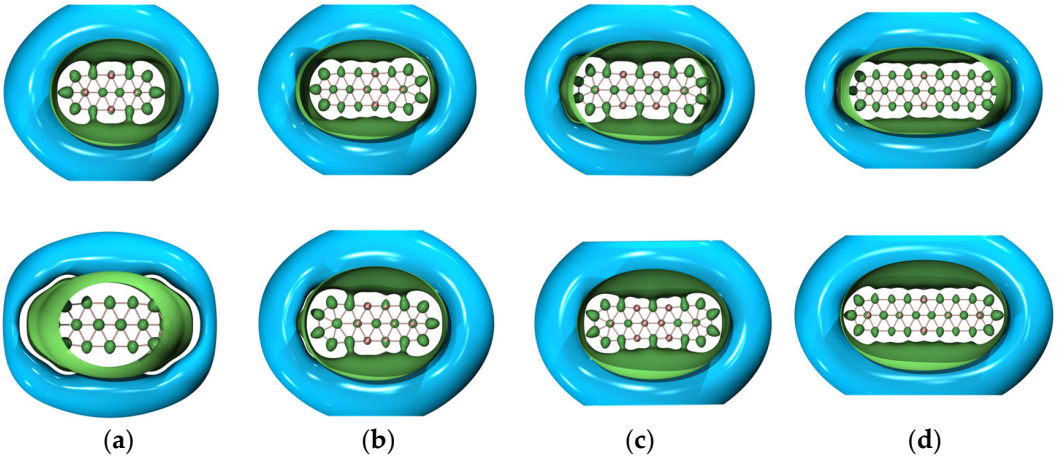

Figure 5. Three-dimensional ICSS maps of both ground- (upper panel) and excited-state (lower panel) (**a**) B_{16}^-, (**b**) B_{20}^-, (**c**) B_{24}^-, and (**d**) B_{28}^-. The isovalue was set to be 0.02 a.u. The inner green surface is positive and the outer cyan surface is negative. Molecular renderings were achieved via the VMD 1.9.4 [55] software.

Table 2. Ground- and excited-state aromaticity of B_{16}^-, B_{20}^-, B_{24}^-, and B_{28}^- in terms of the global NICS values [a].

Species	NICS(0)	NICS(0)$_{ZZ}$	NICS(1)	NICS(1)$_{ZZ}$	NICS(−1)	NICS(−1)$_{ZZ}$
$^2B_{16}^-$	−16.67	−48.74	−17.90	−39.52	−17.90	−39.52
$^4B_{16}^-$	−16.76	−111.92	−5.85	−4.66	−5.83	−4.66
$^2B_{20}^-$	15.51	−28.62	−15.89	−31.60	−11.26	−23.02
$^4B_{20}^-$	22.94	−15.48	−13.61	−32.13	−13.57	−30.98
$^2B_{24}^-$	−29.53	−47.96	−14.42	−26.37	−14.42	−26.37
$^4B_{24}^-$	−26.90	−59.08	−16.85	−38.44	−16.85	−38.44
$^2B_{28}^-$	−18.76	−33.63	−8.27	−16.35	−8.87	−15.98
$^4B_{28}^-$	−17.24	−36.36	−11.94	−22.62	−11.74	−23.33

[a] PBE0/pcJ-2. Units are in ppm. NICS(0) corresponds to the NICS value at the global geometric center, NICS(1) at point 1 Å above the global geometric center, and NICS(−1) at point 1.0 Å below the global geometric center. The *z*-axis component is denoted as NICS$_{ZZ}$.

Hyperfine coupling constants [64,65] provide a direct experimental measure of the distribution of unpaired spin density in paramagnetic molecules. The interactions of unpaired electrons with external magnetic fields arise from the Zeeman effect and from the hyperfine coupling with nuclei having nonzero spins. The latter contribution is related to the chemical environment. For each nucleus N of a molecule located at r_N, the isotropic component of the hyperfine interaction tensor, $a(N)$, is related to the local spin density through [66]

$$a(N) = \frac{8\pi}{3}\beta_e\beta_N g_N \sum_{\mu\nu} P_{\mu\nu}^{\alpha-\beta} \langle \varphi_\mu | \delta(r - r_N) | \varphi_\nu \rangle$$

where β_e, β_N, and g_N are the electronic and nuclear magnetons and the nuclear magnetogiric ratio, the indices μ and ν run over the basis functions, $P_{\mu\nu}^{\alpha-\beta}$ is the difference between the density matrices of spin α and spin β electrons, and $\delta(r - r_N)$ is the Dirac delta function. Therefore, once the density matrices for different spins have been determined, the calculation of $a(N)$ for each nucleus is achieved in a straightforward way. The (isotropic) hyperfine coupling tensor, A_{iso}^N, consists of the Fermi contact term (A_{FC}^N) and a spin orbit correction, the pseudocontact term (A_{PC}^N).

Shown in Table 3 are the isotropic NMR shielding (α_{iso}) constants and hyperfine coupling ($\mathbf{A}_{iso}$) constants for both ground- and excited-state B_{16}^- at the PBE0/pcJ-2 [67,68] level. It is clearly shown that the 16 boron atoms can be roughly grouped into 5 different atoms in different chemical environments as evidenced by both the α_{iso} and $\mathbf{A}_{iso}$ data. Among all the boron atoms, one can easily see that atoms 5 and 6 (as shown in Scheme 1), lying at the two ends of the middle line composed of atoms 1–6, are the most unique. For example, they have the least positive α_{iso} values and the most negative $\mathbf{A}_{iso}$ data. In addition, they undergo the largest changes when going from the ground state to the excited state. Specifically, $\mathbf{A}_{iso}$ changes by ~18 MHz while the largest change of the other atoms is ~8 MHz. Similar trends can be observed for B_{20}^-, B_{24}^-, and B_{28}^- as shown in Tables 4–6.

Table 3. Isotropic NMR shielding constants (α_{iso}, in ppm) and Fermi contact couplings ($\mathbf{A}_{iso}$, in MHz) for ground-state (columns 2, 3, 7, and 8) and excited-state (columns 4, 5, 9, and 10) B_{16}^-.

no.	$^2\alpha_{iso}$	$^2\mathbf{A}_{iso}$	$^4\alpha_{iso}$	$^4\mathbf{A}_{iso}$	no.	$^2\alpha_{iso}$	$^2\mathbf{A}_{iso}$	$^4\alpha_{iso}$	$^4\mathbf{A}_{iso}$
1	77.66	−2.98	78.50	−1.53	9	35.33	40.64	25.78	32.87
2	77.66	−2.98	78.50	−1.56	10	35.34	40.58	25.78	32.86
3	81.47	−5.77	72.32	−8.74	11	69.43	−11.44	82.41	−10.30
4	81.47	−5.77	72.33	−8.74	12	69.42	−11.46	82.41	−10.30
5	8.77	−35.62	36.11	−17.18	13	69.43	−11.44	82.41	−10.30
6	8.77	−35.62	36.11	−17.19	14	69.43	−11.46	82.41	−10.30
7	35.33	40.66	25.78	32.86	15	102.86	−3.11	78.37	0.72
8	35.34	40.60	25.78	32.85	16	102.86	−3.10	78.37	0.72

Table 4. Isotropic NMR shielding constants (α_{iso}, in ppm) and Fermi contact couplings ($\mathbf{A}_{iso}$, in MHz) for ground-state (columns 2, 3, 7, and 8) and excited-state (columns 4, 5, 9, and 10) B_{20}^-.

no.	$^2\alpha_{iso}$	$^2\mathbf{A}_{iso}$	$^4\alpha_{iso}$	$^4\mathbf{A}_{iso}$	no.	$^2\alpha_{iso}$	$^2\mathbf{A}_{iso}$	$^4\alpha_{iso}$	$^4\mathbf{A}_{iso}$
1	82.41	0.71	92.94	1.07	11	39.89	24.08	44.65	13.31
2	75.99	−17.57	64.17	−7.19	12	39.89	24.09	44.53	13.25
3	94.80	5.82	117.43	−0.87	13	26.91	−9.85	30.45	−7.18
4	82.47	−15.30	78.11	−12.48	14	26.91	−9.86	30.46	−7.30
5	18.41	35.48	38.64	35.92	15	78.73	2.80	92.78	2.47
6	78.05	−9.61	74.29	−9.04	16	81.60	−10.16	69.88	−8.16
7	81.60	−10.16	69.82	−8.20	17	69.79	−9.31	79.02	−7.43
8	18.42	35.48	38.84	35.95	18	94.79	5.81	117.62	−0.91
9	34.65	−21.98	19.20	−27.86	19	77.81	4.31	86.55	0.07
10	82.41	0.73	93.02	1.02	20	75.99	−17.58	64.29	−7.26

Table 5. Isotropic NMR shielding constants (α_{iso}, in ppm) and Fermi contact couplings ($\mathbf{A}_{iso}$, in MHz) for ground-state (columns 2, 3, 7, and 8) and excited-state (columns 4, 5, 9, and 10) B_{24}^-.

no.	$^2\alpha_{iso}$	$^2\mathbf{A}_{iso}$	$^4\alpha_{iso}$	$^4\mathbf{A}_{iso}$	no.	$^2\alpha_{iso}$	$^2\mathbf{A}_{iso}$	$^4\alpha_{iso}$	$^4\mathbf{A}_{iso}$
1	80.03	−5.46	79.50	−7.42	13	118.46	−9.58	120.01	−3.83
2	78.34	1.45	79.92	5.62	14	118.46	−9.58	120.01	−3.83
3	83.41	−5.35	88.96	−3.69	15	118.46	−9.58	120.01	−3.83
4	83.41	−5.35	88.96	−3.69	16	68.85	12.02	70.01	4.22
5	78.34	1.45	79.92	5.62	17	68.85	12.02	70.01	4.22
6	80.03	−5.46	79.50	−7.42	18	28.82	−8.41	17.95	−3.84
7	38.44	8.36	45.29	1.03	19	28.82	−8.41	17.95	−3.84
8	66.10	−7.13	64.54	−4.36	20	38.44	8.36	45.29	1.03
9	66.10	−7.13	64.54	−4.36	21	38.44	8.36	45.29	1.03
10	66.10	−7.13	64.54	−4.36	22	28.82	−8.41	17.95	−3.84
11	66.10	−7.13	64.54	−4.36	23	28.82	−8.41	17.95	−3.84
12	118.46	−9.58	120.01	−3.83	24	38.44	8.36	45.29	1.03

Table 6. Isotropic NMR shielding constants (α_{iso}, in ppm) and Fermi contact couplings ($\mathbf{A}_{iso}$, in MHz) for ground-state (columns 2, 3, 7, and 8) and excited-state (columns 4, 5, 9, and 10) B_{28}^-.

no.	$^2\alpha_{iso}$	$^2\mathbf{A}_{iso}$	$^4\alpha_{iso}$	$^4\mathbf{A}_{iso}$	no.	$^2\alpha_{iso}$	$^2\mathbf{A}_{iso}$	$^4\alpha_{iso}$	$^4\mathbf{A}_{iso}$
1	79.30	−7.09	70.30	5.31	15	69.93	−19.78	84.30	0.54
2	73.04	−1.60	84.98	−5.58	16	96.89	31.15	98.54	−1.44
3	83.12	−5.16	78.07	−0.08	17	96.89	31.14	98.57	−1.44
4	84.30	−6.42	78.12	−0.08	18	78.19	−18.49	81.49	−5.32
5	76.95	−3.58	84.99	−5.61	19	74.86	−16.35	81.54	−5.27
6	79.95	−6.84	70.29	5.14	20	74.86	−16.35	81.52	−5.26
7	78.19	−18.49	81.52	−5.34	21	70.58	−4.58	75.02	−5.81
8	82.74	13.22	91.03	−1.62	22	17.52	50.44	29.89	11.67
9	82.74	13.22	90.88	−1.57	23	17.52	50.45	29.91	11.70
10	77.86	17.29	90.69	−1.61	24	37.06	−33.92	16.67	−9.92
11	77.87	17.30	90.80	−1.66	25	63.54	−0.51	74.89	−5.83
12	68.99	−21.28	84.21	0.63	26	42.21	−19.68	16.75	−9.76
13	68.99	−21.28	84.33	0.62	27	14.01	33.86	29.71	11.46
14	69.93	−19.77	84.19	0.55	28	14.00	33.88	29.66	11.45

3. Discussion

Helical frontier molecular orbitals were reported first for hydrocarbon systems, then also for boron-containing molecules [10]. In this work, we have also observed similar results for quasi-planar boron clusters. In addition, as shown in Figure 6, for some other helical (inorganic) motifs, P_9^+, $Be_6B_{11}^-$ (a B_{11} helical structure plus a distorted prism of Be_6), and As_{11}^{3-}, helical frontier molecular orbitals are also observed. Is this helicity a ubiquitous

phenomenon or a special feature of some elements in special molecular topologies? This seems to be an open question, and will be a topic for future research.

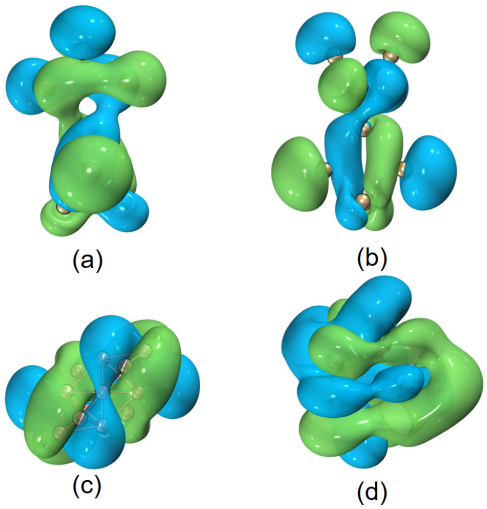

Figure 6. Helical HOMOs of [(**a**,**b**)] P_9^+, (**c**) $Be_6B_{11}^-$, and (**d**) As_{11}^{3-}, respectively. The isovalue was set to be 0.02 a.u. for P_9^+ and 0.01 a.u. for $Be_6B_{11}^-$ and As_{11}^{3-}. Molecular renderings were achieved via the VMD 1.9.4 [55] software.

While a systematic rule for designing molecular templates with helical spin densities is unknown to us, we can show how to elongate the helical frontier molecular orbitals from a given template structure. For example, starting from one conjugated hydrocarbon molecule **1** with helical frontier molecular orbitals, combining two monomers of **1** and a linker, such as $CH_2(\mathbf{1})_2$, $[NH_2(\mathbf{1})_2]^+$, and $[OH(\mathbf{1})_2]^+$, leads to elongated or enlarged helical frontier molecular orbitals as shown in Figure 7. Yet, when three or four monomers of **1** are grouped together, such as $CH(\mathbf{1})_3$ or $C(\mathbf{1})_4$, the helical frontier molecular orbitals are no longer elongated (results not shown). Is it possible to generate an infinite chain of $(\mathbf{1})_\infty$? We do not know; possibly other linkers would work better. For the anionic boron clusters, we failed to even generate a dimer of B_{16}^-; this is presumably because the repulsion between the anionic monomers prevents electron delocalization between them.

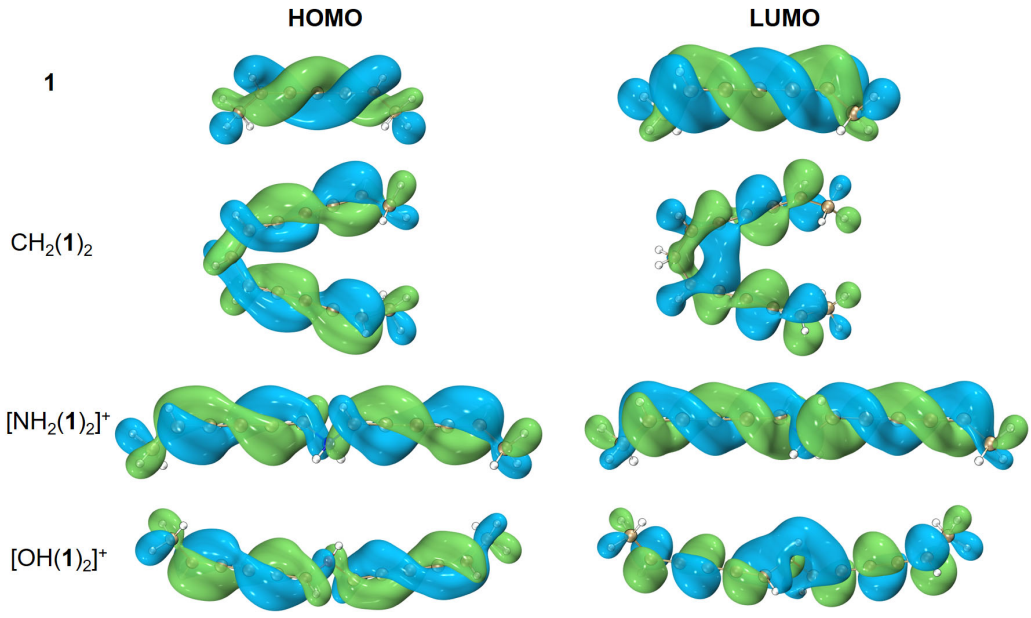

Figure 7. Elongation/enhancement in helical frontier molecular orbitals. The isovalue was set to be 0.02 a.u. Molecular renderings were achieved via the VMD 1.9.4 [55] software.

Finally, we have to point out that in a broader sense, the dissection of chiral boron clusters and the electron spin should be beneficial to its applications to chiral spintronics and materials [69–71].

4. Materials and Methods

To obtain the MPP or SDP values for a molecule, the least square method is used to generate a fitted plane by all the atoms considered. First, one can have a coordinate matrix whose dimension is $3 \times N_{\text{atom}}$. After subtracting out the geometry center, one can easily perform a singular value decomposition for this matrix. To obtain the coefficients (A, B, and C) and constant (D) for a fitting plane $Ax + By + Cz + D = 0$, one can set $A = u_1$, $B = u_2$, $C = u_3$ to be the left singular vectors corresponding to the least singular values. The constant D is determined to be $-(u_1x_c + u_2y_c + u_3z_c)$ if the fitting plane passes through the geometry center (x_c, y_c, z_c) of a molecule. The molecular planarity para meter (MPP) can be readily calculated as the root-mean-squared deviation (RMSD) of the atoms from the fitting plane, $\text{MPP} = \sqrt{\frac{1}{N_{\text{atom}}}\sum_i d_i^2}$, where d_i is the distance between an atom i and the fitting plane, and it can be easily evaluated as $d_i = \frac{|Ax_i+By_i+Cz_i+D|}{\sqrt{A^2+B^2+C^2}}$. The *signed* distance of an atom i to the fitting plane is defined as $d_i^s = \frac{Ax_i+By_i+Cz_i+D}{\sqrt{A^2+B^2+C^2}}$; then, the span of deviation from the plane (SDP) can be calculated as $\text{SDP} = d^s_{\text{max}} - d^s_{\text{min}}$, where $d^s_{\text{max}}/d^s_{\text{min}}$ denote the most positive/negative values of d^s among all considered atoms, respectively.

For all the molecular systems, structure optimization was performed at the density functional theory (DFT) [72,73] PBE0/6-311+G(d) level. Stability of molecular wavefunctions was confirmed via keywords of "guess = mix" and "stable = opt" in Gaussian 16 [74]. Vibrational frequency calculations were ensued to make sure that all the structures were true local minima on the potential energy surface. The optimized atomic Cartesian coordinates are supplied in the Supplementary Materials. Multireference (MR) characteristics of all boron clusters were checked via the T1 diagnostics [75] regarding the coupled cluster theory with single and double substitutions [CCSD/6-311+G(d)] and the frozen core formalism was used for CCSD calculations. The reported values for B_{16}^-, B_{20}^-, B_{24}^-, and B_{28}^- are 0.0365, 0.0495, 0.0344, and 0.0411 for the ground state, and 0.0414, 0.0408, 0.0398, and 0.0367 for the excited state, indicative of non-negligible multi-reference characteristics (because their T1 > 0.02). For the ground state, we also employed a larger basis set cc-pVTZ [76] and very close results were obtained for T1, 0.0360, 0.0488, 0.0344, and 0.0415, respectively. However, for radicals, somewhat larger T1 values (~0.03) are acceptable, and the usual thresholds for T1 are based on accurate quantitative recovery of the dynamic correlation energy, rather than qualitative considerations like those we consider here. The T1 values we report are consistent with the coefficient of the leading determinant being greater than 0.90, implying that single-determinant methods (DFT) and single-reference methods (UCCSD) are good enough to elucidate qualitative features of the boron clusters.

In addition, to force all the atoms to be exactly in a plane, we simply set, for example, the z-components of all the boron atoms to be zero if the original quasi-planar boron cluster is lying in a xy-plane.

To further analyze the aromaticity properties of boron clusters, we employed PBE0/pcJ-2 to calculate the global NICS (nucleus-independent chemical shift) values and GIMIC (gauge-including magnetically induced current) distributions. NMR chemical shielding constants and isotropic hyperfine coupling parameters were obtained at the PBE0/pcJ-2 level with default gauge-including atomic orbitals (GIAOs) [77–81]. The global NICS value is obtained at the geometric center, denoted as NICS(0), and its z-axis component as NICS(0)_{ZZ}. Moreover, another two points (1 Å away from a global center) are also considered and they are signified as NICS(1) and NICS(−1), with their z-axis components denoted as NICS(1)_{ZZ} and $\text{NICS(}-1\text{)}_{ZZ}$.

All DFT calculations were performed by using the Gaussian 16 package with tight self-consistent field (SCF) convergence criteria and ultrafine integration grids to ensure

good accuracy. Multiwfn 3.8 [82] software was used to analyze the planarity of boron clusters and prepare the ICSS input files.

5. Summary

We have observed that helical molecular orbitals and helical spin densities can coexist in a chiral quasi-planar boron cluster. We show that this intriguing phenomenon emerges due to the chiral Jahn–Teller distortion of planar boron clusters and show how to generate elongated or enhanced helical molecular orbitals by grouping building blocks together via a linker. Finally, we found that helical inorganic species have a strong propensity to assume helical molecular orbitals. For potential applications in spintronics, it is interesting to study whether the observed helical spin densities would still be observed for boron clusters adsorbed on metal surfaces. Work along these lines is in progress and the results will be presented elsewhere.

Supplementary Materials: The following supporting information can be downloaded at: https://www.mdpi.com/article/10.3390/molecules29071624/s1, Optimized structures, excited-state VCD spectra, excited-state spin densities, fitted parameters of the planes of boron clusters, and the ground-state spin density maps of planar boron clusters.

Author Contributions: Conceptualization, S.L., P.W.A. and D.Z.; data curation, Y.Z., T.X., X.H., S.H. and D.Z.; formal analysis, Y.Z., T.X., X.H., S.H. and D.Z.; funding acquisition, P.W.A. and D.Z.; project administration, S.L., P.W.A. and D.Z.; supervision, S.L., P.W.A. and D.Z.; writing—original draft, D.Z.; writing—review and editing, S.L., P.W.A. and D.Z. All authors have read and agreed to the published version of the manuscript.

Funding: This work is supported by the National Natural Science Foundation of China (grant no. 22203071), the Yunnan Fundamental Research Projects (grant no. 202101AU070012), the start-up funding of Yunnan University, the High Level Talents Special Support Plan (to D.Z.), NSERC, Canada Research Chairs, and the Digital Research Alliance of Canada.

Institutional Review Board Statement: Not applicable.

Informed Consent Statement: Not applicable.

Data Availability Statement: Data are contained within the article.

Acknowledgments: We are indebted to Benkun Hong and Wei Li and Shuhua Li of the Nanjing University. Part of the computations were performed on the high-performance computers of the Advanced Computing Center of Yunnan University.

Conflicts of Interest: The authors declare no conflicts of interest.

References

1. Krylov, A.I. From orbitals to observables and back. *J. Chem. Phys.* **2020**, *153*, 080901. [CrossRef] [PubMed]
2. Jin, Z.; Li, Y.; Hu, Z.; Hu, B.; Liu, Y.; Iida, K.; Kamazawa, K.; Stone, M.B.; Kolesnikov, A.I.; Abernathy, D.L.; et al. Magnetic molecular orbitals in MnSi. *Sci. Adv.* **2023**, *9*, eadd5239. [CrossRef] [PubMed]
3. Mazin, I.I.; Jeschke, H.O.; Foyevtsova, K.; Valentí, R.; Khomskii, D.I. Na_2IrO_3 as a molecular orbital crystal. *Phys. Rev. Lett.* **2012**, *109*, 197201. [CrossRef]
4. Foyevtsova, K.; Jeschke, H.O.; Mazin, I.I.; Khomskii, D.I.; Valentí, R. Ab initio analysis of the tight-binding parameters and magnetic interactions in Na_2IrO_3. *Phys. Rev. B* **2013**, *88*, 035107. [CrossRef]
5. Streltsov, S.; Mazin, I.I.; Foyevtsova, K. Localized itinerant electrons and unique magnetic properties of $SrRu_2O_6$. *Phys. Rev. B* **2015**, *92*, 134408. [CrossRef]
6. Turco, E.; Bernhardt, A.; Krane, N.; Valenta, L.; Fasel, R.; Juríček, M.; Ruffieux, P. Observation of the Magnetic Ground State of the Two Smallest Triangular Nanographenes. *ACS Au* **2023**, *3*, 1358–1364. [CrossRef] [PubMed]
7. Woodward, R.B.; Hoffmann, R. Stereochemistry of Electrocyclic Reactions. *J. Am. Chem. Soc.* **1965**, *87*, 395–397. [CrossRef]
8. Woodward, R.B.; Hoffmann, R. The Conservation of Orbital Symmetry. *Angew. Chem. Int. Ed.* **1969**, *8*, 781–853. [CrossRef]
9. Hoffmann, R.; Woodward, R.B. Conservation of orbital symmetry. *Acc. Chem. Res.* **1968**, *1*, 17–22. [CrossRef]
10. Hendon, C.H.; Tiana, D.; Murray, A.T.; Carbery, D.R.; Walsh, A. Helical frontier orbitals of conjugated linear molecules. *Chem. Sci.* **2013**, *4*, 4278–4284. [CrossRef]
11. Imamura, A.; Aoki, Y. Helical molecular orbitals around straight-chain polyyne oligomers as models for molecular devices. *Chem. Phys. Lett.* **2013**, *590*, 136–140. [CrossRef]

12. Liu, M.; Artyukhov, V.I.; Lee, H.; Xu, F.; Yakobson, B.I. Carbyne from First Principles: Chain of C Atoms, a Nanorod or a Nanorope. *ACS Nano* **2013**, *7*, 10075–10082. [CrossRef]
13. Garner, M.H.; Hoffmann, R.; Rettrup, S.; Solomon, G.C. Coarctate and Möbius: The Helical Orbitals of Allene and Other Cumulenes. *ACS Cent. Sci.* **2018**, *4*, 688–700. [CrossRef] [PubMed]
14. Garner, M.H.; Jensen, A.; Hyllested, L.O.; Solomon, G.C. Helical orbitals and circular currents in linear carbon wires. *Chem. Sci.* **2019**, *10*, 4598–4608. [CrossRef] [PubMed]
15. Orimoto, Y.; Aok, Y.; Imamura, A. Extraction of One-Handed Helical Frontier Orbital in Even [*n*]Cumulenes by Breaking Mirror Images of Right- and Left-Handed Helical Orbitals: Theoretical Study. *J. Phys. Chem. C* **2019**, *123*, 11134–11139. [CrossRef]
16. Garner, M.H.; Laplaza, R.; Corminboeuf, C. Helical versus linear Jahn–Teller distortions in allene and spiropentadiene radical cations. *Phys. Chem. Chem. Phys.* **2022**, *24*, 26134–26143. [CrossRef]
17. Ozcelik, A.; Aranda, D.; Gil-Guerrero, S.; Pola-Otero, X.A.; Talavera, M.; Wang, L.; Behera, S.K.; Gierschner, J.; Peña-Gallego, Á.; Santoro, F.; et al. Distinct Helical Molecular Orbitals through Conformational Lock. *Chem. Eur. J.* **2020**, *26*, 17342–17349. [CrossRef] [PubMed]
18. Garner, M.H.; Corminboeuf, C. Correlation between Optical Activity and the Helical Molecular Orbitals of Allene and Cumulenes. *Org. Lett.* **2020**, *22*, 8028–8033. [CrossRef] [PubMed]
19. Pinter, P.; Munz, D. Controlling Möbius-Type Helicity and the Excited-State Properties of Cumulenes with Carbenes. *J. Phys. Chem. A* **2020**, *124*, 10100–10110. [CrossRef]
20. Garner, M.H.; Corminboeuf, C. Helical electronic transitions of spiroconjugated molecules. *Chem. Commun.* **2021**, *57*, 6408–6411. [CrossRef]
21. Bro-Jørgensen, W.; Garner, M.H.; Solomon, G.C. Quantification of the Helicality of Helical Molecular Orbitals. *J. Phys. Chem. A* **2021**, *125*, 8107–8115. [CrossRef] [PubMed]
22. Bro-Jørgensen, W.; Solomon, G.C. Understanding Current Density in Molecules Using Molecular Orbitals. *J. Phys. Chem. A* **2023**, *127*, 9003–9012. [CrossRef] [PubMed]
23. Gunasekaran, S.; Venkataraman, L. Tight-binding analysis of helical states in carbyne. *J. Chem. Phys.* **2020**, *153*, 124304. [CrossRef] [PubMed]
24. Aoki, Y.; Orimoto, Y.; Imamura, A. One-Handed Helical Orbitals in Conjugated Molecules. *ACS Cent. Sci.* **2018**, *4*, 664–665. [CrossRef] [PubMed]
25. Gückel, S.; Gluyas, J.B.G.; El-Tarhuni, S.; Sobolev, A.N.; Whiteley, M.W.; Halet, J.-F.; Lapinte, C.; Kaupp, M.; Low, P.J. Iron versus Ruthenium: Clarifying the Electronic Differences between Prototypical Mixed-Valence Organometallic Butadiyndiyl Bridged Molecular Wires. *Organometallics* **2018**, *37*, 1432–1445. [CrossRef]
26. Honda, S.; Sugawara, R.; Ishida, S.; Iwamoto, T. A Spiropentasiladiene Radical Cation: Spin and Positive Charge Delocalization across Two Perpendicular Si=Si Bonds and UV–vis–NIR Absorption in the IR-B Region. *J. Am. Chem. Soc.* **2021**, *143*, 2649–2653. [CrossRef]
27. Barber, J.S.; Yamano, M.M.; Ramirez, M.; Darzi, E.R.; Knapp, R.R.; Liu, F.; Houk, K.N.; Garg, N.K. Diels-Alder cycloadditions of strained azacyclic allenes. *Nat. Chem.* **2018**, *10*, 953–960. [CrossRef]
28. Ramirez, M.; Svatunek, D.; Liu, F.; Garg, N.K.; Houk, K.N. Origins of Endo Selectivity in Diels-Alder Reactions of Cyclic Allene Dienophiles. *Angew. Chem. Int. Ed.* **2021**, *60*, 14989–14997. [CrossRef]
29. Balakrishnan, A.; Vijayakumar, S. Highly delocalised molecular orbitals in boron-, carbon- and nitrogen-based linear chains: A DFT study. *Mol. Phys.* **2022**, *120*, e2020923. [CrossRef]
30. Baronas, P.; Komskis, R.; Tankelevičiu Tė, E.; Adomėnas, P.; Adomėnienė, O.; Juršėnas, S. Helical Molecular Orbitals to Induce Spin–Orbit Coupling in Oligoyne-Bridged Bifluorenes. *J. Phys. Chem. Lett.* **2021**, *12*, 6827–6833. [CrossRef]
31. Albert, B.; Hillebrecht, H. Boron: Elementary Challenge for Experimenters and Theoreticians. *Angew. Chem. Int. Ed.* **2009**, *48*, 8640–8668. [CrossRef] [PubMed]
32. Zhao, D.; He, X.; Li, M.; Wang, B.; Guo, C.; Rong, C.; Chattaraj, P.K.; Liu, S. Density functional theory studies of boron clusters with exotic properties in bonding, aromaticity and reactivity. *Phys. Chem. Chem. Phys.* **2021**, *23*, 24118–24124. [CrossRef] [PubMed]
33. Xu, S.; He, C.; Zhao, Y.; Yang, X.; Xu, H. Generalized Octet Rule with Fractional Occupancies for Boron. *J. Am. Chem. Soc.* **2023**, *145*, 25003–25009. [CrossRef] [PubMed]
34. Zhang, W.; Zhao, Y.; An, X.; Fu, J.; Zhang, J.; Zhao, D.; Liu, S.; Rong, C. Cooperativity and reactivity properties of medium-sized boron clusters: A combined density functional theory and information-theoretic approach study. *Mol. Phys.* **2022**, e2157774. [CrossRef]
35. Sergeeva, A.P.; Zubarev, D.Y.; Zhai, H.; Boldyrev, A.I.; Wang, L. A Photoelectron Spectroscopic and Theoretical Study of B_{16}^- and B_{16}^{2-}: An All-Boron Naphthalene. *J. Am. Chem. Soc.* **2008**, *130*, 7244–7246. [CrossRef]
36. Kiran, B.; Bulusu, S.; Zhai, H.; Yoo, S.; Zeng, X.; Wang, L. Planar-to-tubular structural transition in boron clusters: B_{20} as the embryo of single-walled boron nanotubes. *Proc. Natl. Acad. Sci. USA* **2005**, *102*, 961–964. [CrossRef] [PubMed]
37. Popov, I.A.; Piazza, Z.A.; Li, W.; Wang, L.; Boldyrev, A.I. A combined photoelectron spectroscopy and ab initio study of the quasi-planar B_{24}^- cluster. *J. Chem. Phys.* **2013**, *139*, 144307. [CrossRef]
38. Wang, Y.; Zhao, Y.; Li, W.; Jian, T.; Chen, Q.; You, X.; Ou, T.; Zhao, X.; Zhai, H.; Li, S.; et al. Observation and characterization of the smallest borospherene, B_{28}^- and B_{28}. *J. Chem. Phys.* **2016**, *144*, 064307. [CrossRef] [PubMed]

39. Von Barth, U.; Hedin, L. A Local Exchange-Correlation Potential for the Spin Polarized Case: I. *J. Phys. C Solid State Phys.* **1972**, *5*, 1629. [CrossRef]
40. Gunnarsson, O.; Lundqvist, B.I. Exchange and Correlation in atoms, molecules and solids by the spin-density-functional formalism. *Phys. Rev. B* **1976**, *13*, 4274–4298. [CrossRef]
41. Rajagopal, A.K.; Callaway, J. Inhomogeneous electron gas. *Phys. Rev. B* **1973**, *7*, 1912–1919. [CrossRef]
42. Ayers, P.W.; Yang, W. Legendre-transform functionals for spin-density-functional theory. *J. Chem. Phys.* **2006**, *124*, 224108. [CrossRef] [PubMed]
43. Galván, M.; Vargas, R. Spin Potential in Kohn—Sham Theory. *J. Phys. Chem.* **1992**, *96*, 1625–1630. [CrossRef]
44. Ghanty, T.K.; Ghosh, S.K. Spin-Polarized Generalization of the Concepts of Electronegativity and Hardness and the Description of Chemical Binding. *J. Am. Chem. Soc.* **1994**, *116*, 3943–3948. [CrossRef]
45. Garza, J.; Vargas, R.; Cedillo, A.; Galván, M.; Chattaraj, P.K. Comparison between the frozen core and finite differences approximations for the generalized spin-dependent global and local reactivity descriptors in small molecules. *Theor. Chem. Acc.* **2006**, *115*, 257–265. [CrossRef]
46. Pérez, P.; Chamorro, E.; Ayers, P.W. Universal mathematical identities in density functional theory: Results from three different spin-resolved representations. *J. Chem. Phys.* **2008**, *128*, 204108. [CrossRef] [PubMed]
47. Ayers, P.W.; Fias, S.; Heidar-Zadeh, F. The axiomatic approach to chemical concepts. *Comput. Theor. Chem.* **2018**, *1142*, 83–87. [CrossRef]
48. Liu, S. Conceptual Density Functional Theory and Some Recent Developments. *Acta Phys-Chim. Sin.* **2009**, *25*, 590–600.
49. Johnson, P.A.; Bartolotti, L.J.; Ayers, P.W.; Fievez, T.; Geerlings, P. Charge density and chemical reactivity: A unified view from conceptual DFT. In *Modern Charge Density Analysis*; Gatti, C., Macchi, P., Eds.; Springer: Berlin/Heidelberg, Germany, 2012; pp. 715–764.
50. Geerlings, P.; Chamorro, E.; Chattaraj, P.K.; De Proft, F.; Gázquez, J.L.; Liu, S.; Morell, C.; Toro-Labbé, A.; Vela, A.; Ayers, P.W. Conceptual density functional theory: Status, prospects, issues. *Theor. Chem. Acc.* **2020**, *139*, 36. [CrossRef]
51. Jissy, A.K.; Datta, A. What Stabilizes the Li_nP_nInorganic Double Helices? *J. Phys. Chem. Lett.* **2013**, *4*, 1018–1022. [CrossRef]
52. Guo, J.; Feng, L.; Wang, Y.; Jalife, S.; Vásquez-Espinal, A.; Cabellos, J.L.; Pan, S.; Merino, G.; Zhai, H. Coaxial Triple-Layered versus Helical $Be_6B_{11}^-$ Clusters: Dual Structural Fluxionality and Multifold Aromaticity. *Angew. Chem. Int. Ed.* **2017**, *56*, 10174–10177. [CrossRef] [PubMed]
53. Reber, A.C.; Ugrinov, A.; Sen, A.; Qian, M.; Khanna, S.N. Helical and linear $[K(As_{11})]^{2-}$ chains: Role of solvent on the conformation of chains formed by Zintl anions. *Chem. Phys. Lett.* **2009**, *473*, 305–311. [CrossRef]
54. Lu, T. Simple, reliable, and universal metrics of molecular planarity. *J. Mol. Model.* **2021**, *27*, 263. [CrossRef] [PubMed]
55. Humphrey, W.; Dalke, A.; Schulten, K. VMD: Visual molecular dynamics. *J. Mol. Graph.* **1996**, *14*, 33–38. [CrossRef] [PubMed]
56. Adamo, C.; Barone, V. Toward reliable density functional methods without adjustable parameters: The PBE0 model. *J. Chem. Phys.* **1999**, *110*, 6158–6169. [CrossRef]
57. McLean, A.D.; Chandler, G.S. Contracted Gaussian-basis sets for molecular calculations. 1. 2nd row atoms, Z=11-18. *J. Chem. Phys.* **1980**, *72*, 5639–5648. [CrossRef]
58. Dennington, R.D., II; Keith, T.A.; Millam, J.M. *GaussView 6.0.16*; Semichem, Inc.: Shawnee, KS, USA, 2016.
59. Jusélius, J.; Sundholm, D.; Gauss, J. Calculation of current densities using gauge-including atomic orbitals. *J. Chem. Phys.* **2004**, *121*, 3952–3963. [CrossRef] [PubMed]
60. Fliegl, H.; Taubert, S.; Lehtonen, O.; Sundholm, D. The gauge including magnetically induced current method. *Phys. Chem. Chem. Phys.* **2011**, *13*, 20500–20518. [CrossRef] [PubMed]
61. Schleyer, P.v.R.; Maerker, C.; Dansfeld, A.; Jiao, H.; Hommes, N.J.R.v.E. Nucleus-Independent Chemical Shifts: A Simple and Efficient Aromaticity Probe. *J. Am. Chem. Soc.* **1996**, *118*, 6317–6318. [CrossRef]
62. Kloda, S.; Kleinpeter, E. Ab initio calculation of the anisotropy effect of multiple bonds and the ring current effect of arenes—Application in conformational and configurational analysis. *J. Chem. Soc. Perkin Trans.* **2001**, *2*, 1893–1898.
63. Ahrens, J.; Geveci, B.; Law, C. ParaView: An End-User Tool for Large Data Visualization. In *Visualization Handbook*; Elesvier: Amsterdam, The Netherlands, 2005.
64. Rega, N.; Cossi, M.; Barone, V. Development and validation of reliable quantum mechanical approaches for the study of free radicals in solution. *J. Chem. Phys.* **1996**, *105*, 11060–11067. [CrossRef]
65. Barone, V. Electronic, vibrational and environmental effects on the hyperfine coupling constants of nitroside radicals. H_2NO as a case study. *Chem. Phys. Lett.* **1996**, *262*, 201–206. [CrossRef]
66. Golding, R.M.; Stubbs, L.C. The Evaluation of the Hyperfine Interaction Tensor Components in Molecular Systems. *Proc. R. Soc. Lond. A.* **1977**, *354*, 223–244.
67. Jensen, F. The Basis Set Convergence of Spin−Spin Coupling Constants Calculated by Density Functional Methods. *J. Chem. Theory Comput.* **2006**, *2*, 1360–1369. [CrossRef] [PubMed]
68. Pritchard, B.P.; Altarawy, D.; Didier, B.; Gibson, T.D.; Windus, T.L. A New Basis Set Exchange: An Open, Up-to-date Resource for the Molecular Sciences Community. *J. Chem. Inf. Model.* **2019**, *59*, 4814–4820. [CrossRef] [PubMed]
69. Naaman, R.; Paltiel, Y.; Waldeck, D.H. Chiral Molecules and the Electron Spin. *Nat. Rev. Chem.* **2019**, *3*, 250–260. [CrossRef]
70. Yang, S.-H.; Naaman, R.; Paltiel, Y.; Parkin, S.S.P. Chiral spintronics. *Nat. Rev. Phys.* **2021**, *3*, 328–343. [CrossRef]

71. Liu, Y.; Xiao, J.; Koo, J.; Yan, B. Chirality-driven topological electronic structure of DNA-like materials. *Nat. Mater.* **2021**, *20*, 638–644. [CrossRef] [PubMed]
72. Parr, R.G.; Yang, W. *Density Functional Theory of Atoms and Molecules*; Oxford University Press: Oxford, UK, 1989.
73. Teale, A.M.; Helgaker, T.; Savin, A.; Adamo, C.; Aradi, B.; Arbuznikov, A.V.; Ayers, P.W.; Baerends, E.J.; Barone, V.; Calaminici, P.; et al. DFT exchange: Sharing perspectives on the workhorse of quantum chemistry and materials science. *Phys. Chem. Chem. Phys.* **2022**, *24*, 28700–28781. [CrossRef]
74. Frisch, M.J.; Trucks, G.W.; Schlegel, H.B.; Scuseria, G.E.; Robb, M.A.; Cheeseman, J.R.; Scalmani, G.; Barone, V.; Petersson, G.A.; Nakatsuji, H.; et al. *Gaussian 16 Revision C.01*; Gaussian Inc.: Wallingford, CT, USA, 2016.
75. Lee, T.J.; Taylor, P.R. A diagnostic for determining the quality of single-reference electron correlation methods. *Int. J. Qunantum Chem.* **1989**, *36*, 199–207. [CrossRef]
76. Dunning, T.H., Jr. Gaussian basis sets for use in correlated molecular calculations. I. The atoms boron through neon and hydrogen. *J. Chem. Phys.* **1989**, *90*, 1007–1023. [CrossRef]
77. London, F. The quantic theory of inter-atomic currents in aromatic combinations. *J. Phys. Radium* **1937**, *8*, 397–409. [CrossRef]
78. McWeeny, R. Perturbation Theory for Fock-Dirac Density Matrix. *Phys. Rev.* **1962**, *126*, 1028–1034. [CrossRef]
79. Ditchfield, R. Self-consistent perturbation theory of diamagnetism. 1. Gauge-invariant LCAO method for N.M.R. chemical shifts. *Mol. Phys.* **1974**, *27*, 789–807. [CrossRef]
80. Wolinski, K.; Hinton, J.F.; Pulay, P. A Comparison of Models for Calculating Nuclear Magnetic Resonance Shielding Tensors. *J. Am. Chem. Soc.* **1990**, *112*, 8251–8260. [CrossRef]
81. Cheeseman, J.R.; Trucks, G.W.; Keith, T.A.; Frisch, M.J. A comparison of models for calculating nuclear magnetic resonance shielding tensors. *J. Chem. Phys.* **1996**, *104*, 5497–5509. [CrossRef]
82. Lu, T.; Chen, F. Multiwfn: A multifunctional wavefunction analyzer. *J. Comput. Chem.* **2011**, *33*, 580–592. [CrossRef]